SUPPLEMENT TO THE *WELDING JOURNAL*, OCTOBER 2009
Sponsored by the American Welding Society and the Welding Research Council

Transient High-Frequency Welding Simulations of Dual-Phase Steels

Numerical and experimental simulations were used to investigate high-frequency welding of advanced high-strength steels

BY R. BAUMER AND Y. ADONYI

ABSTRACT

Continued development of advanced high-strength steel (AHSS) requires a corresponding improvement in joining technology. One promising joining method is high-frequency butt joint welding. Seeking to validate the utility of this process for joining AHSS flat sheet specimens for steel mill processing lines, high-frequency butt joint welding of flat sheet steel was investigated through a combined numerical and experimental simulation methodology. Simulated welds were produced and pre-Curie and post-Curie temperature heating rate differences were observed with infrared radiation (IR) imaging. Good correlations were found between numerical predictions and actual heating rates. Final metallographic analysis revealed complete coalescence of faying surface, with only minor hardening at the weld interface. It was concluded that high-frequency welding shows good potential for coil joining in steel processing lines.

Introduction

Modern steel coil processing lines (such as pickling and galvanizing) benefit greatly from a continuous feed of steel strip, a process that requires coil end joining (Ref. 1). As is shown in Fig. 1, continuous processing is achieved through the combined use of an accumulator (Fig. 1B) (Ref. 2) and a coil end welding machine (Fig. 1C). Due to the finite capacity of the accumulator, one main constraint on welding process selection is welding speed. Additional constraints, such as material thickness, result in a variety of welding processes being used for coil end joining, including gas tungsten arc welding (GTAW), gas metal arc welding (GMAW), flash welding (FW), resistance (mash) seam welding (RSEW-MS), and laser beam welding (LBW) (Ref. 3). Note that the last two are mostly used on tin coating and recoiling lines, where the sheet thickness is less than 1 mm.

Joining of advanced high-strength steel (AHSS) coil ends brings additional challenges to coil end joining due to inherent high strength, prompting difficulties in end shearing, and faying surface alignment, and a propensity for localized hardening in welding microstructures. Indeed, excessive hardness in the fusion and heat-affected zones has been reported in the case of laser beam welding of dual-phase (DP) and transformation-induced plasticity (TRIP) steels (Ref. 4). The presence of such excessive hardness can provide a metallurgical notch, precipitating joint failure during subsequent mill operations. To eliminate potential problems stemming from the as-cast microstructures found in fusion welding, a solid-state welding process is desired for joining AHSS coil ends. While resistance welding (RW) and flash welding (both solid-state processes) are currently widely employed in coil joining, RW is slow and is limited to small thicknesses (Ref. 1) while FW can be difficult to control because it is susceptible to irregular arcing and incomplete fusion on the strip edges. Even resultant strip breaks of 0.2% are not acceptable, as equipment is damaged and production lost. Therefore, an improved solid-state joining process is desired for joining AHSS coil ends.

Previous work has demonstrated that a coupled high-frequency induction heating/pressure welding (termed hyper-interfacial bonding) operation can produce faying surface coalescence in butt joint configurations and minimize thermally induced changes in grain size of ultrafine-grained steel (Ref. 5). Heating times for $5 \times 5 \times 30$-mm specimens were shown to be very rapid (0.2 s to 1600°C at 1 MHz and 50–59 kW) (Ref. 5), indicating that high-frequency welding can satisfy the time constraints associated with coil end joining.

Additionally, previous research demonstrated that high-frequency welding could produce good welds in AHSS specimens (Fig. 2), as evidenced by successful limited dome height formability testing (Ref. 6). The long history of successful high-frequency induction welding (HFIW) of joints in tubular products and structural shapes (Ref. 7) also suggests the usefulness of high-frequency welding for coil end joining.

This present work builds on this foundation by developing numerical and experimental techniques for simulating high-frequency welding of dual-phase steel coil ends, thereby 1) providing insight into fundamental high-frequency heating/material interactions, 2) establishing operating parameters, and 3) demonstrating the feasibility of joining DP steel coil ends with high-frequency welding.

KEYWORDS

High-Frequency Welding
Dual-Phase Steels
FEA Modeling
Heating Rates

Physical Simulation Overview

High-frequency induction heating/pressure welding of dual-phase steels was performed at small scale through induction heating using a solid-state-controlled, state-of-the-art 100-kW variable-frequency (250–400 kHz) induction welding power supply. After heating specimens to forging

R. BAUMER is a Graduate Student at Massachusetts Institute of Technology, Cambridge, Mass. Y. ADONYI is the Omer Blodgett Professor of Welding and Materials Joining Engineering at LeTourneau University, Longview, Tex.

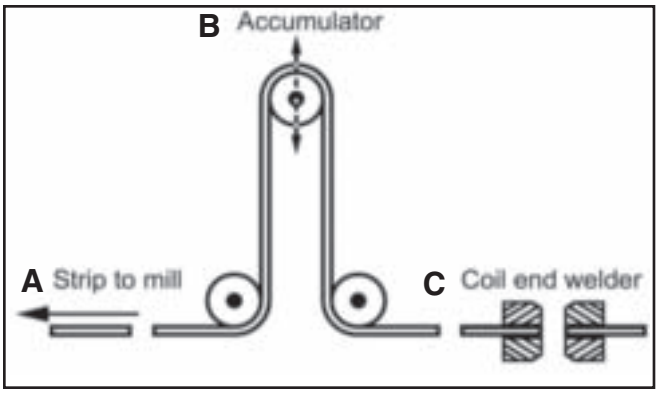

Fig. 1 — Schematic representation of accumulator and coil end welding machine utilized in continuous steel strip processing mills. A — Strip to mill; B — accumulator — moving vertical rollers allow for a varying amount of strip to be stored, enabling the stored strip to be fed to the mill line while keeping the coil end stationary; C — welding machine utilized to join the end of the coil in the mill and the lead end of the next coil. (Fig. 1B reproduced after Ref. 2 with permission from MetalForming/PMA Services, Inc.)

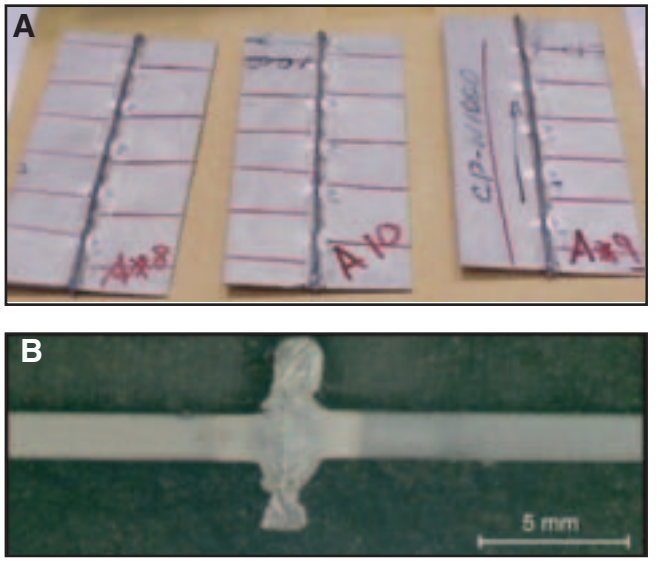

Fig. 2 — High-frequency welds made in advanced high-strength steels (different composition than the DP600 but still possessing near 600 MPa ultimate tensile strength). A — As-welded specimens; B — transverse micrograph. Previously published in Ref. 6. Used with permission from US Steel Research Europe, Kosice, Slovak Republic.

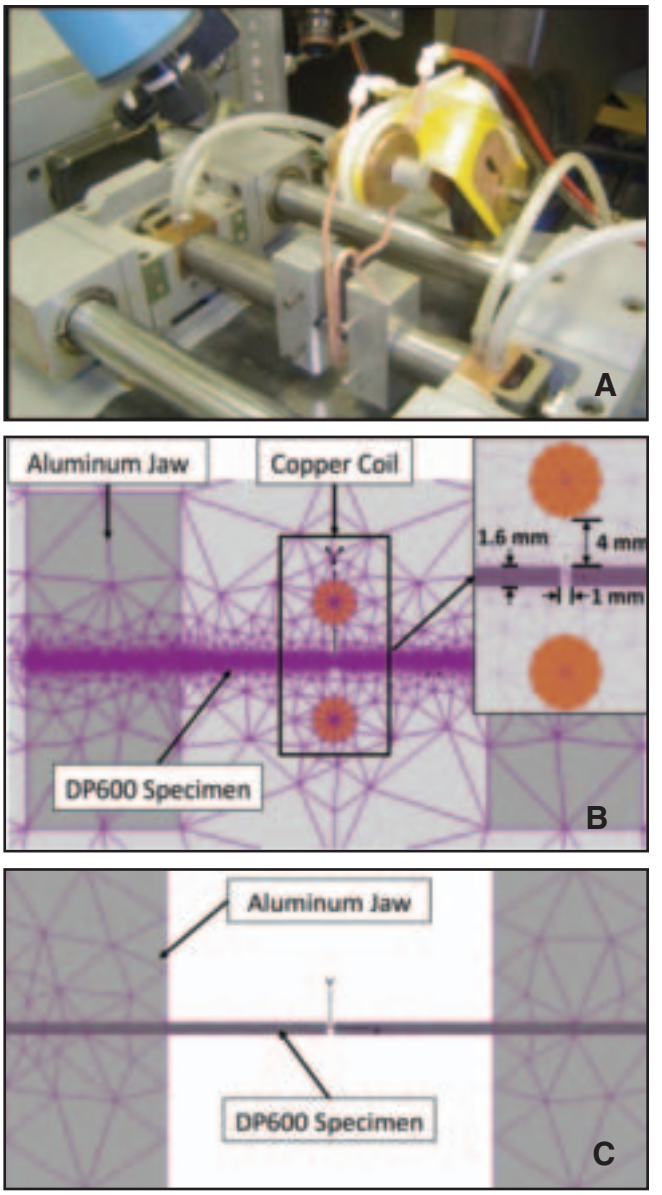

Fig. 3 — A — Physical simulation setup. Note results reported in this present investigation utilized a single-turn induction coil and did not use the two-turn coil shown above; B — electromagnetic model simulation geometry with representative mesh density; C — thermal model simulation geometry with representative mesh density.

temperatures and turning off the induction coil power supply, controlled deformation was delivered by the hydraulic ram system of a connected Gleeble 1500® thermomechanical simulator. All heating and deformation timing was precisely controlled via a LabVIEW control program connecting the two systems. Small-scale welding specimens (1.5 × 44 × 89 mm) were rigidly constrained in aluminum jaws and heated by a water-cooled, copper induction coil — Fig. 3A. Atmospheric shielding was accomplished by flooding the welding chamber with argon.

As compared to the industry standard high-frequency resistance welding (HFRW) often employed in tube welding (Ref. 7), the experimental simulation technique reported here is distinguished by 1) a transient process unable to reach the steady-state operating condition characteristic of HFRW, 2) controlled relative motion between faying surfaces (i.e., not dependent upon the speed or V angle of the advancing pipe), and 3) variable frequency between 250 and 400 kHz using the latest solid-state power control technology.

Fundamentals of the Heating Mechanisms

Heating of welding specimen edges prior to forging is the consequence of both eddy current heating, accentuated by the skin effect, and hysteresis heating (ferromagnetic materials only). Eddy current heating occurs due to resistive heating losses accompanying induced current flow in a material. By consequence of the skin effect, current distributions are restricted to shallow penetration depths on faying surfaces, leading to rapid heating and high efficiencies (Ref. 8). For ferromagnetic materials, hysteresis heating also occurs, a direct consequence of inelastic magnetization/demagnetization (represented by the area enclosed by the BH curve of a material) (Ref. 9). Naturally, hysteresis heating ceases when the Curie temperature (approximately 1033 K for ferromagnetic materials) (Ref. 10) is reached and materials become paramagnetic.

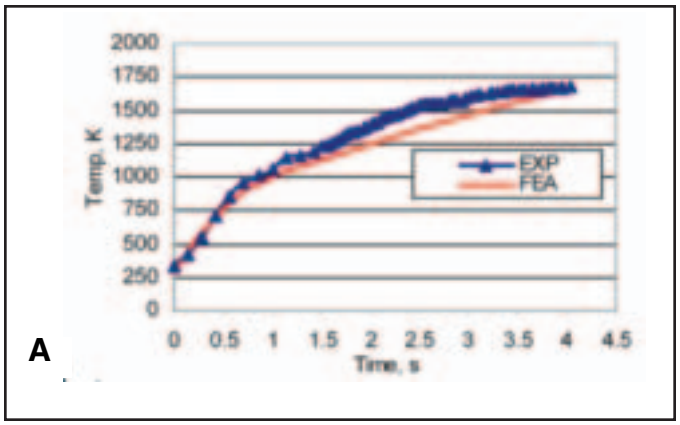

Fig. 4 — A — Comparison of numerical and experiment temperatures; B — heating rates vs. time at the faying surface (weld interface center). Numerical simulation results for DP600 heated with a 1750-A induction coil current input (315 kHz). Physical experimental results shown for DP600 welded at 315 kHz and 40 kW.

Table 1 — Material Input Parameters for Numerical Simulations of High-Frequency Induction Heating of DP600 Sheet Steel

Temp. K	Thermal Conductivity W·m⁻¹·K⁻¹	Temp. K	Specific Heat J·kg⁻¹·K⁻¹	Temp. K	Resistivity μΩ·m	Magnetic Loss W·kg⁻¹	B Field T	H Amp·m⁻¹	293 K μ_r	523 K μ_r	773 K μ_r	1023 K μ_r
273	59.5	323	450	273	0.3	0.00	0	0	0.0	0.0	0.0	0.0
373	57.8	473	520	373	0.38	5512	0.015	100	11.0	9.2	6.7	1.9
473	53.2	573	565	473	0.44	22050	0.03	200	16.6	13.8	10.0	2.9
573	49.4	623	590	573	0.42	49612	0.045	300	20.3	17.0	12.3	3.6
673	45.6	723	650	673	0.65	88200	0.06	400	23.2	19.4	14.1	4.2
773	41	823	730	773	0.78	137812	0.075	500	25.5	21.3	15.5	4.7
873	36.8	973	825	873	0.92	198450	0.09	1000	35.2	29.5	21.6	6.8
973	33.1	1023	1100	973	1.11	270112	0.105	2000	44.8	37.7	27.9	9.4
1073	28.5	1073	875	1073	1.34	352800	0.12	3000	50.7	42.9	31.9	11.4
1273	27.6	1123	846	1173	1.55	446512	0.135	4000	55.2	46.8	35.2	13.2

Note: Thermal conductivity values were taken from SAE 1008 carbon steel (Ref. 18); specific heat capacity values were taken from SAE 1010 (323–1023 K) and SAE 1008 (1073–1123 K) (Ref. 16). Resistivity values were determined using DP980 (Ref. 17). Magnetic loss was determined at 280 kHz using Equation 9. Relative magnetic permeability was determined using Equation 10.

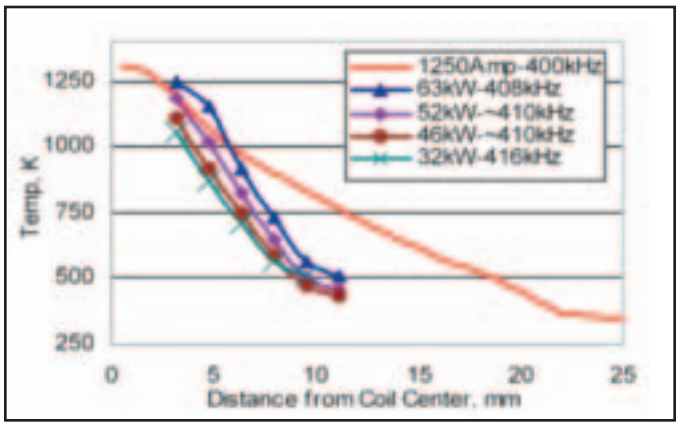

Fig. 5 — Comparison of numerical and experiment temperature distributions. Experimental data obtained through static heating trials of DP600.

Fundamentals of the Deformation Mechanisms

Weld quality in high-frequency welding is strongly dependent upon the nature of deformation at the faying surface. Previous research indicates that control of deformation input parameters of total faying surface upset, deformation strain rate, and forging operation temperatures can improve coalescence of faying surfaces during high-frequency welding of high-performance steels (HPS) (Ref. 11). While the significance of these mechanisms is certainly recognized in this present research, neither total upset nor deformation rates were considered as primary variables in this initial process development, as fundamental heating parameters were of primary concern.

Objectives

The purpose of this numerical and physical simulation study was to understand and characterize the thermal phenomena governing the bond quality in transient high-frequency joining of DP steels. The study was also intended to validate the concept of designing a steel coil joining prototype and provide means to link parametric effects found at small scale to future full-scale implementation.

Methodology

Induction Heating Simulation Overview

Induction heating is modeled by solving both the electromagnetic response to current flow through the heating coil and the thermal response of the specimen to eddy current and hysteresis heating. The electromagnetic regime is described by Maxwell's equations and associated constitutive relations (as given by Ref. 15)

$$\vec{\nabla} \cdot \vec{B} = 0 \qquad (1)$$

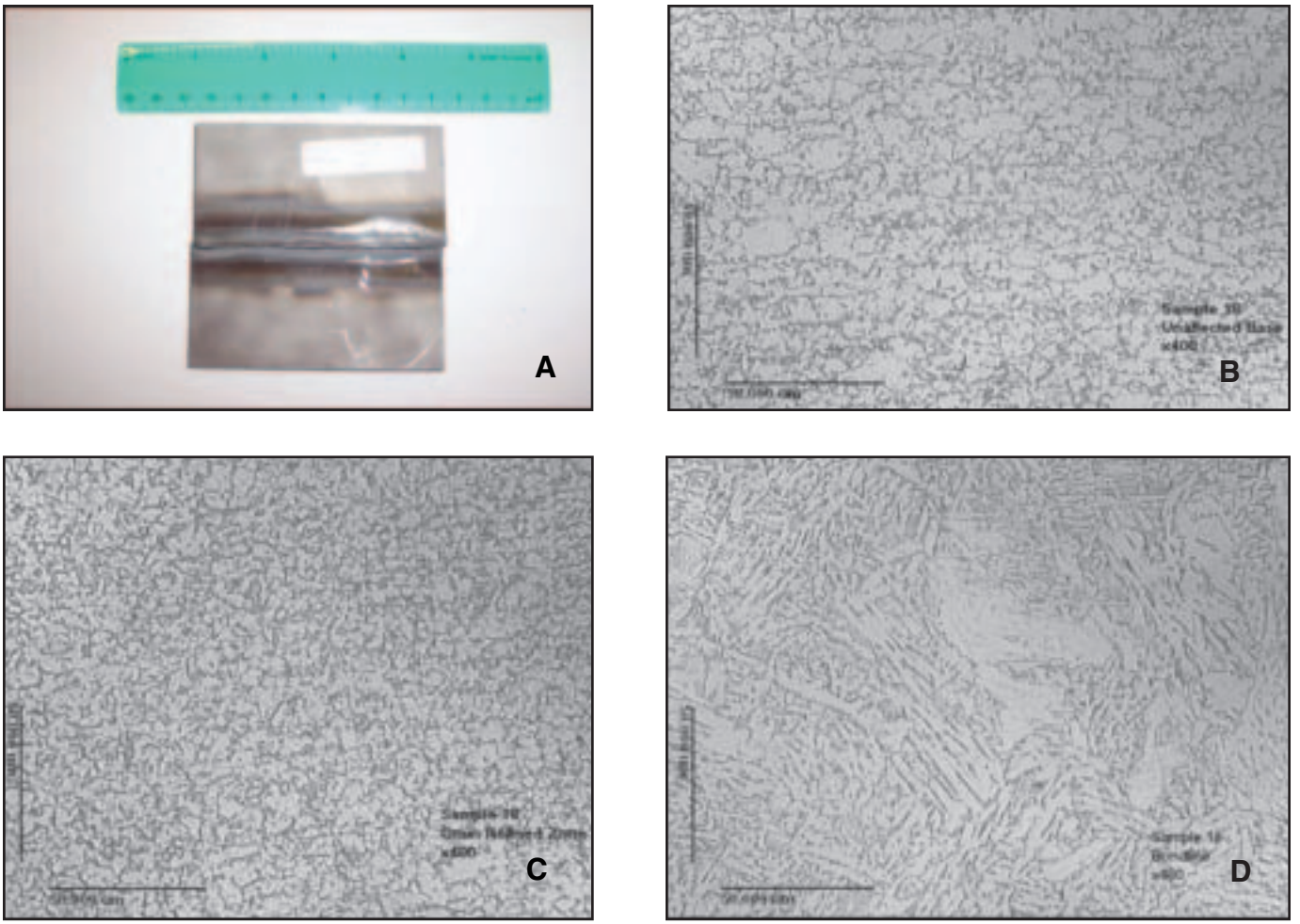

Fig. 6 — Sample 18: DP 600, 42 kW, 315 kHz, 4 s heating. A — Welded sample; B — base metal; C — grain-refined zone; D — weld interface.

$$\vec{\nabla} \cdot \vec{D} = 0 \quad (2)$$

$$\vec{\nabla} \times \vec{E} = -\frac{\partial \vec{B}}{\partial t} \quad (3)$$

$$\vec{\nabla} \times \vec{H} = \vec{J} + \frac{\partial \vec{D}}{\partial t} \quad (4)$$

$$\vec{D} = \varepsilon \vec{E} \quad (5)$$

$$\vec{B} = \mu \vec{H} \quad (6)$$

$$\vec{J} = \sigma \vec{E} \quad (7)$$

where B is magnetic induction, D is electric flux density, E is electric field strength, H is magnetic field strength, μ is magnetic permeability, ε is dielectric constant, and σ is conductivity.

Solutions in the electromagnetic regime yield eddy current and hysteresis power losses, which comprise the thermal generation term in the generalized heat equation (Refs. 12, 15)

$$\vec{\nabla} \cdot \left(k \nabla T\right) + \dot{Q} = \rho C \frac{\partial T}{\partial t} \quad (8)$$

where $\dot{Q}$ is internal heat generation (in this problem, coming from hysteresis and eddy current power losses), k is thermal conductivity, ρ is density, and C is specific heat.

Solving the heat equation yields the resulting temperature distribution in the specimen. Due to the temperature dependence of all material properties, coupling between the governing equations is highly nonlinear, requiring a numerical solution method. (Refer to Refs. 9 and 12–15 for detailed explanations of the governing equations and associated numerical solutions.)

In this present work, a systematic numerical simulation of induction heating of flat sheet DP steels was conducted using the commercial finite element analysis (FEA) software MagNet and ThermNet from Infolytica Corp. MagNet enables a user to model components and current-carrying conductors (using a CAD-type interface) and solve for the resulting electromagnetic field interaction between the two via an FEA-based solution method. Solutions include static, time-harmonic, and transient responses in two or three dimensions. Similarly, ThermNet provides an FEA-based solution to the transient thermal response of a component subject to heating or cooling phenomenon. Solutions include static and transient responses in two or three dimensions. Induction heating is modeled by solving electromagnetic and thermal systems together.

Numerical Simulation: Specimen Geometry, Mesh, and Boundary Conditions

Model geometry was defined in two dimensions only, operating under the assumption that edge heating effects were negligible. Dual-phase steel welding specimens were each said to be 1.6 mm thick and 43.5 mm in length, with a 1-mm root opening between faying surfaces. The induction coil was modeled as a solid copper conductor of 6.35 mm diameter with a liftoff of 4 mm. Aluminum jaws utilized to contain specimens during physical trials were also included in the model — Fig. 3B. Simulations were conducted in a simulation cell (referred to as the AirBox) of dimensions 176 × 176 mm.

Following the definition of specimen

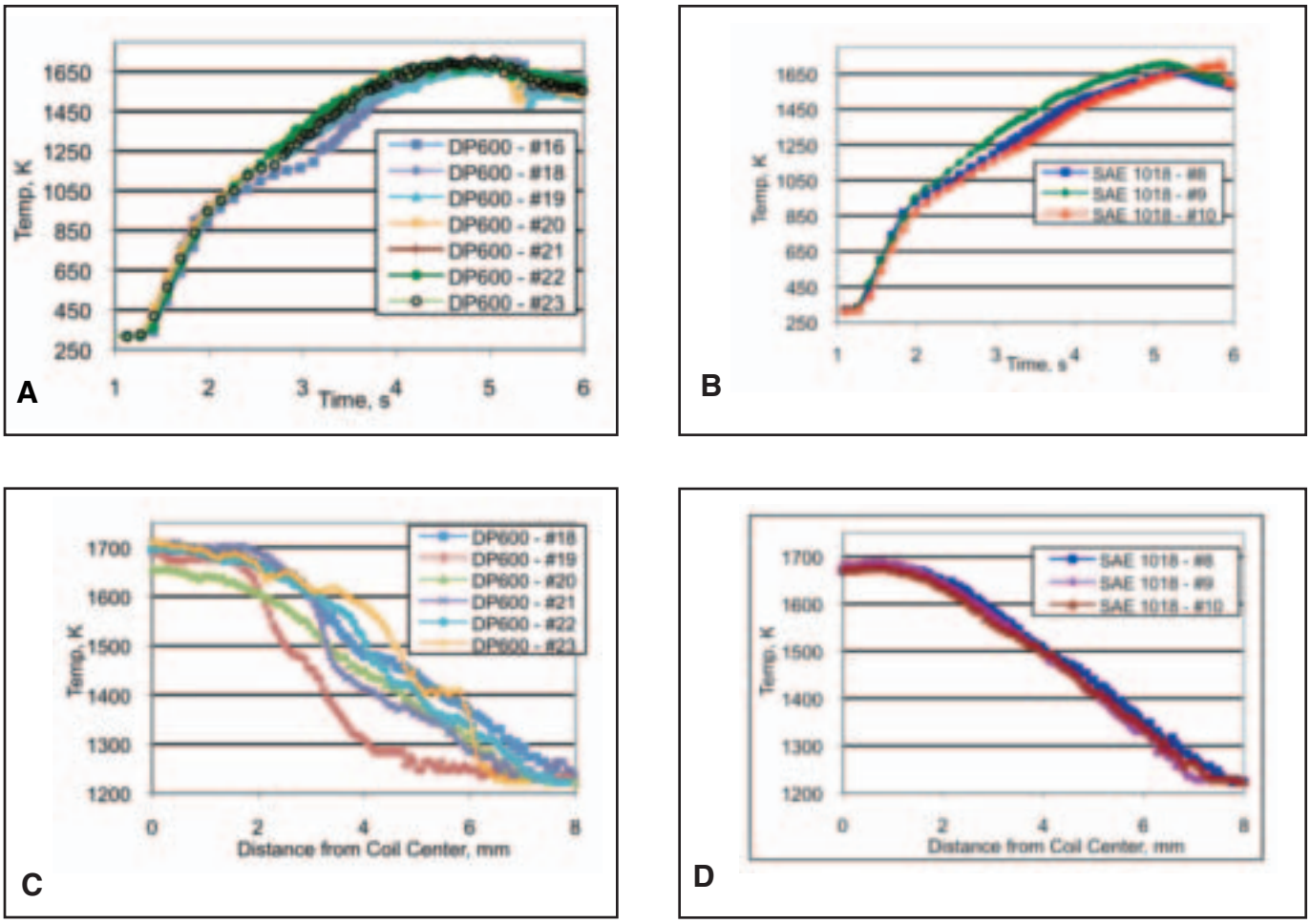

Fig. 7 — A — Temperature evolution at the weld interface for DP600; B — temperature evolution at the weld interface for SAE 1018; C — temperature distribution at time of maximum temperature (immediately prior to upset) of DP600; D — temperature distribution at time of maximum temperature (immediately prior to upset) of SAE 1018.

Table 2 — Representative Physical Simulation Input Parameters for DP600 and SAE 1018

Material	Frequency kHz	Power kW	Gap mm	Liftoff mm	Upset mm	Disp. Rate mm s^{-1}	Trial Time s
SAE 1018	316	42	1	4	–1	10	4
DP 600	315	42	1	4	–2	100	4
SAE 1018	403	42	1	4	–2	20	4
DP 600	398	42	1	4	–2	20	4

Note: See Appendix 1 for all data.

geometry, the second step in FEA implementation was spatial discretization. In the electromagnetic model, due to the rapidly changing electromagnetic fields, the maximum element size (MES) in the sample was to be no larger than 0.25 mm. No MES was specified for the AirBox or the coil, and the computer generated one appropriate to the geometry — Fig. 3C. For the thermal model, no maximum element size was set for any part of the model, and an appropriate mesh was automatically generated — Fig. 3C. A polynomial order of two was set for all element equations.

The electromagnetic boundary conditions were set to have flux lines tangential to the AirBox perimeter and at the intersection of the AirBox with the sheet specimen. This facilitated the approximation that the sheet specimen was being inductively heated in an infinitely large volume. In the thermal regime, the adiabatic boundary condition was applied to all surfaces, assuming that radiative and convective heat losses were small compared to conduction of heat within the specimen.

Numerical Simulation: Material Properties

Material properties requiring definition for successful FEA simulation of induction heating are mass density, thermal conductivity, specific heat, electrical resistivity (or conductivity), magnetic loss (hysteresis loss), magnetic permeability, and electric permittivity. Mass density was taken to be 7600 kg·m^3. Thermal conductivity and specific heat were determined through handbook data for low-carbon steel (Ref. 16), with the values defined as shown in Table 1. Electrical resistivity as a function of temperature was measured through a modified form of ASTM B-193 (Ref. 17) (Table 1). While simulations were based on resistivity data collected on

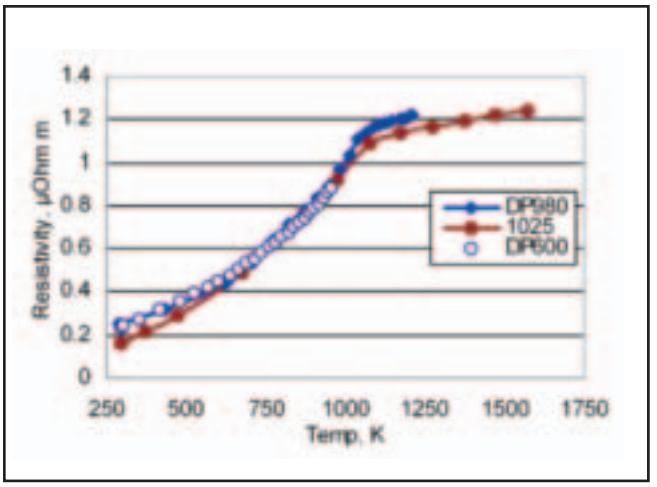

Fig. 8 — Resistivity vs. temperature profiles for DP600, DP980, and SAE 1025. Resistivity data for SAE 1025 taken from Ref. 16. Resistivity of DP steels determined through a modified form of ASTM B193-02 (Ref. 17).

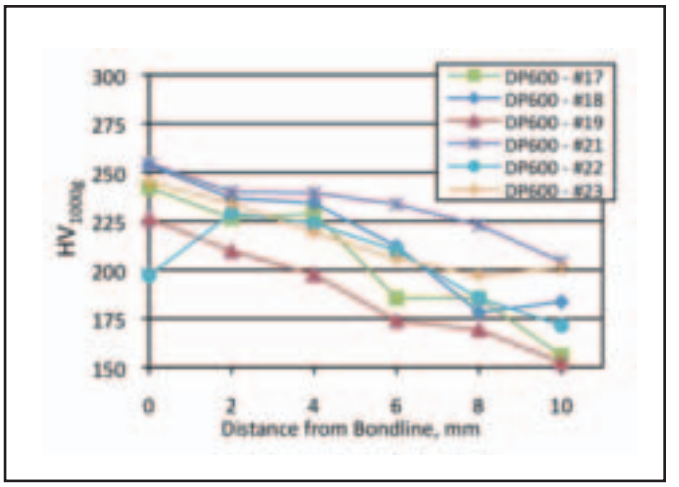

Fig. 9 — Hardness data on DP600 high-frequency welding simulation specimens.

DP980, additional resistivity testing of DP600 demonstrated the values to be nearly identical — Fig. 8. Magnetic loss was determined through the empirically based Steinmetz equation (Ref. 18):

$$< P_{\nu}\left(t\right) >= C \cdot f^{\alpha} \cdot B^{\gamma} \quad (9)$$

where $<P_{\nu}(t)>$ is the average power loss per volume; C, α, and γ are constants (set equal to 87500, 1, and 2, respectively); f is frequency; and B is the peak magnetic induction. Magnetic permeability was found through the following equation

$$\mu_r\left(H,T\right) = 1 + \sqrt{\left(T_c - T\right) \cdot k_1} \times \frac{k_2}{k_2 + H} \quad (10)$$

where μ_r is the relative magnetic permeability, k_1 and k_2 are constants (set equal to 10 and 100, respectively); and T_c is the Curie temperature. Magnetic induction (B-field) was subsequently determined by treating μ as the first derivative of the B-H curve and performing numerical integration (Ref. 15).

In the initial stages of material property definition, experimentally obtained heating profiles of DP steel at low powers (1 kW) were utilized to optimize the correlation between numerical and experimental simulation heating profiles. Assuming that hysteresis heating dominates the heating mechanism before the Curie temperature, hysteresis loss was treated as a correction factor and the constants of Equation 1 were iteratively adjusted until an optimal correlation was obtained with experimental heating curves. Following material property definition, high-power simulations were conducted (1000–1750 A_{rms} coil current input, 250–400 kHz, and 4.5 s heating time). A complete list of material input properties for DP600 is provided in Table 1. Electromagnetic models were solved using the time-harmonic approximation (material nonlinearities were still considered) while the thermal mode was solved for the transient solution. A time step of 0.25 s was used in the electromagnetic model, while a 0.10 s time step was utilized in the thermal model.

Experimental Simulation Methodology

Dual-phase steel and SAE 1018 carbon steel specimens (1.5 mm thick) were water cut to 1.75 × 3.5 in. (44.45 × 88.9 mm), sandblasted, and painted with high-temperature HiE-Coat™ 840-M paint (Ref. 19), designed to ensure consistent material emissivity and corresponding infrared radiation (IR) camera accuracy. Welds were made on both DP and carbons steel, with the primary operating parameters being 4-mm coil liftoff, 42 kW, 315 kHz, and a 1-mm root opening (Table 2). During heating, the transient thermal response was collected via two digital IR cameras, which provided (when operated together) an accurate measure of a range of temperatures between 298 and 1733 K. Data collected with these two cameras enabled temperature evolution at the weld interface and temperature distributions transverse to faying surfaces to be measured. Following welding, metallurgical analysis was performed using optical microscopy and Vickers microhardness indentation (1000-g load and 12-s dwell time). Selected specimens were cross sectioned transverse to the weld interface, mounted, prepared to a 1.0 μm final polish, and chemically etched using 2% Nital etch.

Results

Numerical Simulation

Temperature evolution profiles for the faying surface of DP600 specimens (FEA simulation at 1750 A_{rms} input current and 315 kHz) clearly indicated the distinct heating mechanisms occurring before and after the Curie temperature — Fig. 4A. Before the Curie temperature (~1033 K), heating rates are as high as 1000 K s^{-1}. After the Curie temperature, heating rates drop to approximately 225 K s^{-1}, a decrease of approximately 75% — Fig. 4B. Comparison with physical simulation results indicates that the numerical values fall within approximately 10% of the experimental data, emphasizing that the dramatic decrease in heating rate after the Curie temperature observed in our numerical simulations is indeed a real result.

While heating profiles at the faying surface correspond well between the numerical and physical simulations, temperature distribution comparisons (sampled at the peak temperature in static heating trials) reveal a growing divergence (with increasing distance from the weld interface) between the numerical and experimental temperature distributions — Fig. 5. Divergence between numerical and experimental simulations in the transverse heating profiles suggests that our material property values could be further refined. We consider Equations 9 and 10 to be the most likely source of this divergence, especially since Equation 10 deviates somewhat from formulations given in the literature (Refs. 13, 15). However, the accurate temperature evolution profiles indicate that our general methodology is sound, and we anticipate that future re-

Table 3 — Summary of Statistical Analysis

	Pre-Curie Temp Heating Rate Ks^{-1}		Post-Curie Temp Heating Rate Ks^{-1}		Max. Temp. K	
Mean	DP 600	SAE 1018	DP 600	SAE 1018	DP 600	SAE 1018
Mean	904.9	786.0	227.6	225.6	1697.6	1692.5
St. Dev.	62.8	68.0	25.1	42.2	8.9	27.2
Observations	8	9	25.1	42.2	7	3
df	15		13		2	
Hypo. Dif.	60		0		0	
t Stat	1.856		0.122		0.317	
t Stat-Critical	1.753		1.77		2.920	
1 Tail P Value	0.04		0.45		0.390	
DP 600>SAE 1018 by	7.6%		0%		0%	
with Confidence	96%		—		—	

Table 4 — Composition Information

	C	Mn	P	S	Si	Cr	Mo	Al	N	Ti	Other
1.52 mm DP 600 GN (Ref. 23)	0.084	1.50	0.009	0.0073	0.010	0.032	0.315	0.054	0.017	<0.002	V = 0.003 Cu = 0.037
AISI 1018 (Ref. 24)	0.15–0.20	0.60–0.90	≤0.04	≤0.05	0.15–0.30	—	—	—	—	—	Cu ≥0.20

finement of model material properties (particularly magnetic loss and permeability) could improve results.

Physical Simulation

Both SAE 1018 and DP600 steel sheet specimens (1.6 × 44 × 89 mm) were welded at the parameters in Table 2, successful welds being produced in all cases — Fig. 6. During welding, IR thermal imaging of specimens was obtained, enabling the determination of temperature evolution of the weld interface and temperature distributions transverse to the weld interface (measured right before the weld plunge).

Curie Temperature Effect on Heating Rate

Analysis of the continuous heating profiles (Fig. 7) indicates a striking difference in heating rate before and after the Curie temperature (inflection point in the heating curve), similar to the results obtained through numerical simulations. This difference was the expected result due to the sudden change in heating mechanism upon reaching the Curie temperature. The magnitude of the heating rate differences was significant, with the post-Curie temperature heating rate being nearly 75% less than the pre-Curie temperature heating rates (~225 K s^{-1} vs. ~900 K s^{-1}).

Heating Rate Comparisons between DP600 and SAE 1018

In addition to a difference in heating rate before and after the Curie temperature, comparison of continuous heating profiles between DP600 and SAE 1018 welding specimens revealed a noticeable difference (also observed qualitatively during experiments) in induction heating response. Statistical analysis performed using a one-sided t-test (data assumed to be normally distributed and variances assumed to be unequal) indicated a statistically significant difference between the mean heating rates for DP600 and SAE 1018. For mean pre-Curie temperature heating rates, DP600 was shown to be 7.6% greater than SAE 1018 at a 96% confidence level (Table 3). However, post-Curie temperature heating rates and maximum temperatures were not shown to have any statistically significant differences.

The lack of a statistically significant difference in heating rate after the Curie temperature indicates that heating arising from resistive losses is essentially the same in the two materials, prompting the supposition that the difference in heating rate between DP600 and SAE 1018 must arise from a difference in the magnetic response of each material. Support for this conjecture is supported first by the similarity in resistivity vs. temperature profiles for dual-phase and carbon steel (Fig. 8) (Refs. 16, 17). Secondly, such an explanation is bolstered by the reported sensitivity of the magnetization response of materials to their composition and microstructural differences (Refs. 20–22). Considering that compositions (Table 4) (Refs. 23, 24) and microstructures (by definition of a dual-phase vs. plain carbon steel) are different between DP600 and SAE 1018, the magnetization response ought to be different between the two materials, as was observed experimentally.

Metallography

Microstructure analysis of the DP600 specimens revealed grain coarsening at the weld interface, indicating that upset was not sufficient to expel the thermally affected base metal completely from the weld interface — Fig. 6. Microhardness profiles across the welding zone indicated a slight hardening at the weld interface — Fig. 9. However, in an extreme case of failure to upset the cast microstructure, hardness at the weld interface was double those values found in other specimens, underscoring the importance of sufficient upset to displace unwanted material from the faying surfaces.

Deformation Response

A maximum force of approximately 275 kN was measured at the faying surfaces, indicating that a maximum pressure of 20 MPa ensured faying surface coalescence and upset.

Conclusions

1) Fundamental induction heating mechanisms were revealed through a combined numerical and physical simulation effort. Specifically, in both DP600 and

SAE 1018 (ferromagnetic) materials, heating rates were found to be significantly different before and after the Curie temperature. Additionally, induction heating rates were found to be dependent on the ferromagnetic material type.

2) Satisfactory simulated welds can be produced in sheet steel specimens at 42 kW, 315 kHz, and heating for 4 s with 1-mm root opening (gap) between faying surfaces. This result demonstrates that high-frequency induction heating/pressure welding could serve as an excellent solid-state joining process for use in joining steel coil ends in continuous coil processing mills.

3) The usefulness of the coupled numerical and experimental simulation technique was clearly evidenced by the insights gained into the high-frequency induction heating process.

Additional study of this new process is certainly warranted and successful realization of a full-scale prototype of the joining process is optimistically anticipated.

Acknowledgments

The financial support of this work by the 2007 AISI/FeMETGrant and US Steel Europe R&D sponsorship is gratefully acknowledged. We also thank Prof. Robert Warke for his invaluable contributions to the project, as well as the following LeTourneau University students: Caleb Mellbom, Jordan Smith, Josh Swenson, Stevenson Jian, Jack Dunaway, Jerica Cadman, Jody Carter, Mitch Plant, and Steve Wolbert.

References

1. Halmos, G. T., ed. 2006. *Roll Forming Handbook.* Boca Raton, Fla.: CRC Press.

2. Steinmeyer, L. 1999. Accumulate uptime by joining coils. *Metalforming* magazine. *http://archive.metalforming magazine.com/1999/01/coilkent/coils.htm*.

3. Shaffer, S. 2003. Coil joining criteria for tube and pipe mills. *Tube & Pipe Journal*, *www.thefabricator.com/TubePipe Production/TubePipeProduction_Article.cfm?ID=260*.

4. Kang, C.-Y., Han, T.-K., Lee, B.-K., and Kim, J.-K. 2007. Characteristics of Nd:YAG

Appendix 1 — Data Table

Table 5 — Summary of Data Collected during April 10, 2008, Trial

Spec. Num	Mat.	Freq.	Power	Root Opening Size	Upset	Disp. Rate	Forge Delay	Set Trial Time	Liftoff	Time to Max. Temp.	Max. Temp.	Pre-Curie Temp. Heating Rate	Post-CurieTemp. Heating Rate
No.		kHz	kW	mm	mm	mm s^{-1}	s	s	mm	s	K	K s^{-1}	K s^{-1}
1	1018	310	300 set			0		1.0	4	?	?	744	388
2	1018	317	42	0.5	0	0		2.0	4	2.4	?	929	265
3	1018	317	42	0.5	0	0		2.5	4	2.8	1505	840	310
4	1018	317	42	1	0	0		2.5	4	2.7	1434	696	301
5	1018	317	42	1.5	0	0		2.5	4	2.5	1401	794	273
6	1018	317	42	1	0	0		3.0	4	3.0	1539	837	286
7	1018	317	42	1	0	0		3.5	4	3.9	1628	724	232
8	1018	317	42	1	0	0		4.0	4	4.2	1661	787	205
9	1018	318	42	1	0	0		4.0	4	4.0	1706	807	212
10	1018	316	42	1	–1	10		4.0	4	4.7	1710	694	196
11	1018	316	42	1	–1	10	–0.25	4.8	4	3.8	1707	889	226
12	1018	317	42	1	–1	10	–0.25	4.8	4	4.4	1714	806	200
13	DP 600	315	42	1	–2	20	–0.25	4.75	4	4.0	1731	969	250
14	1018	316	42	1	–1	100	–0.25	4.5	4	4.7	1706	836	172
15	DP 600	315	42	1	–1	20	–0.25	4.5	4	?	1688	?	240
16	DP 600	313	42	1	–1	20	–0.25	4	4	3.9	1698	831	219
17	DP 600	309	42	1	–2	20	–0.25	4	4	?	1715	?	242
18	DP 600	308	42	1	–1	100	–0.25	4	4	4.2	1701	965	207
19	DP 600	315	42	1	–2	100	–0.25	4	4	4.2	1679	915	185
20	DP 600	319	42	1	–1	20	–0.25	4	4	3.7	1697	923	216
21	DP 600	319	42	1	–2	20	–0.25	4	4	3.6	1697	959	236
22	DP 600	318	42	1	–1	100	–0.25	4	4	3.3	1703	872	259
23	DP 600	318	42	1	–2	100	–0.25	4	4	3.7	1707	805	248
24	1018	403	42	1	–2	20	–0.25	4	4	4.6	1695	692	224
25	DP 600	398	42	1	–2	20	–0.25	4	4	3.6	1670	755	226

Frequency, root opening size, upset, displacement rate, forge delay, set trial time, and liftoff were input parameters. Time to maximum temperature, maximum temperature, pre-Curie temperature heating rate, and post-Curie temperature heating rate were determined via analysis of IR thermal imaging.

laser welded 600 MPa grade TRIP and DP steels. *Proc. 5th International Conference on Processing and Manufacturing of Advanced Materials — THERMEC' 2006*. Vancouver, Canada, pp. 3967–3972.

5. Saida, K., Jeong, B., and Nishimoto, K. 2004. Development of hyper-interfacial bonding technique for ultra-fine grained steels and microstructural analysis of bonded joints. *Science and Technology of Welding and Joining* 9 (6): 548–554.

6. Adonyi, Y., Jurko, V., and Lesko, A. 2007. Modeling and characterization of high-frequency induction welds in advanced high strength steels. *Proc. AIST steel properties and applications conference*, Combined with Ms and T07, Materials Science and Technology. Detroit, Mich., pp. 195–206.

7. Smith, W., and Roberts, J. 1993. High-frequency welding. Welding, brazing and soldering. *ASM Handbook* Vol. 6, pp. 252, 253. Materials Park, Ohio, ASM International.

8. Choi, J.-H., Chang, Y.-S., Kim, C.-M., Oh, J.-S., and Kim, Y.-S. 2004. Penetrator formation mechanisms during high-frequency electric resistance welding. *Welding Journal* 83 (1): 27-s to 31-s.

9. Garbulsky, G. D., Marino, P., and Pignotti, A. 1997. Numerical modeling of induction heating of steel-tube ends. *IEEE Transactions on Magnetics* 33(1): 746–52.

10. Lindgren, Art. 1989. Magnetic particle inspection. Nondestructive evaluation and quality control. *ASM Handbook* Vol. 17, p. 89. Materials Park, Ohio: ASM International.

11. Swenson, J., Adonyi, Y., and Warke, R. 2008. Deformation effects during variable high-frequency welding of modern steels. *Proc. 8th International Conference on Trends in Welding Research*, Pine Mountain, Ga. (in-press).

12. Skoczkowski, T. P., and Kalus, M. F. 1989. Mathematical model of induction heating of ferromagnetic pipes. *IEEE Transactions on Magnetics* 25(3): 2745–2750.

13. Chaboudez, C., Clain, S., Glardon, R., Rappaz, J., Swierkosz, M., and Touzani, R. 1994. Numerical modeling of induction heating of long workpieces. *IEEE Transactions on Magnetics* 30(6): 5028–5037.

14. Kim, H.-J., and Youn, S.-K. 2008. Three dimensional analysis of high-frequency induction welding of steel pipes with impeder. *Journal of Manufacturing Science and Engineering, Transactions of the ASME* 130(3): 031005-1 to 031005-7.

15. Favennec, Y., Labbe, V., Tillier, Y., and Bay, F. 2002. Identification of magnetic parameters by inverse analysis coupled with finite-element modeling. *IEEE Transactions on Magnetics* 38(6): 3607–3619.

16. 2002. Physical properties of carbon and low-alloy steels. Properties and selection: Irons, steels, and high performance alloys. 10th ed. *ASM Handbook* Vol. 1, pp. 195–199. Materials Park, Ohio: ASM International.

17. ASTM B193-02. *Standard Test Method for Resistivity of Electrical Conductor Materials*. West Conshohocken, Pa.: ASTM International.

18. Li, J., Abdallah, T., and Sullivan, C. R. 2001. Improved calculation of core loss with nonsinusoidal waveforms. *Proc. Industry Applications Conference*, 36th IAS annual meeting. Chicago, Ill., pp. 2203–2210.

19. Aremco Products, Inc. 2008. High Temperature Specialty Coatings, technical bulletin A5. Valley Cottage, N.Y. *www.aremco.com/PDFs/A5_08.pdf*.

20. Ryu, K. S., Nahm, S. H., Kim,Y. B., Yu, K. M., and Son, D. 2000. Dependence of magnetic properties on isothermal heat treatment time for 1Cr-1Mo-0.25V steel. *Journal of Magnetism and Magnetic Materials* 222(1-2): 128–32.

21. Martinez-de-Guerenu, A., Gurruchaga, K., and Arizti, F. 2007. Nondestructive characterization of recovery and recrystallization in cold rolled low carbon steel by magnetic hysteresis loops. *Journal of Magnetism and Magnetic Materials* 316(2): 842–845.

22. Kupferling, M., Appino, C., Basso,V., Bertotti, G., Fiorillo, F., and Meilland, P. 2007. Magnetic hysteresis in plastically deformed low-carbon steel laminations. *Journal of Magnetism and Magnetic Materials* 316(2): e842–e845.

23. Auto/Steel Partnership. 2007. Advanced high strength steel (AHSS) weld performance study for autobody structural components. *www.a-sp.org/publications.htm*.

24. AISI 1018. *Alloy Digest*. ASM International, Materials Park, Ohio, p. 2002.

Preparation of Manuscripts for Submission to the *Welding Journal* Research Supplement

All authors should address themselves to the following questions when writing papers for submission to the Welding Research Supplement:

- Why was the work done?
- What was done?
- What was found?
- What is the significance of your results?
- What are your most important conclusions?

With those questions in mind, most authors can logically organize their material along the following lines, using suitable headings and subheadings to divide the paper.

1) **Abstract.** A concise summary of the major elements of the presentation, not exceeding 200 words, to help the reader decide if the information is for him or her.

2) **Introduction.** A short statement giving relevant background, purpose, and scope to help orient the reader. Do not duplicate the abstract.

3) **Experimental Procedure, Materials, Equipment.**

4) **Results, Discussion.** The facts or data obtained and their evaluation.

5) **Conclusion.** An evaluation and interpretation of your results. Most often, this is what the readers remember.

6) **Acknowledgment, References and Appendix.**

Keep in mind that proper use of terms, abbreviations, and symbols are important considerations in processing a manuscript for publication. For welding terminology, the *Welding Journal* adheres to AWS A3.0:2001, *Standard Welding Terms and Definitions.*

Papers submitted for consideration in the Welding Research Supplement are required to undergo Peer Review before acceptance for publication. Submit an original and one copy (double-spaced, with 1-in. margins on 8 ½ x 11-in. or A4 paper) of the manuscript. A manuscript submission form should accompany the manuscript.

Tables and figures should be separate from the manuscript copy and only high-quality figures will be published. Figures should be original line art or glossy photos. Special instructions are required if figures are submitted by electronic means. To receive complete instructions and the manuscript submission form, please contact the Peer Review Coordinator, Erin Adams, at (305) 443-9353, ext. 275; FAX 305-443-7404; or write to the American Welding Society, 550 NW LeJeune Rd., Miami, FL 33126.